CrossMark

REVIEW

X-ray diffraction and X-ray absorption spectroscopic analyses for intercalative nanohybrids with low crystallinity

Dae-Hwan Park [a,1]**, Jae-Hun Yang** [a,1]**, Ajayan Vinu** [b]**, Ahmed Elzatahry** [c,d]**,**
Jin-Ho Choy [a,b,*]

[a] *Center for Intelligent Nano Bio Materials (CINBM), Department of Chemistry and Nano Science, Ewha Womans University, Seoul 120-750, Republic of Korea*
[b] *Australian Institute for Bioengineering and Nanotechnology (AIBN), The University of Queensland, Brisbane 4072, Australia*
[c] *Materials Science and Technology Program, College of Arts and Sciences, Qatar University, P.O. Box 2713, Doha, Qatar*
[d] *Department of Chemistry, Petrochemicals Research Chair, King Saud University, P.O. Box 2455, Riyadh 11451, Saudi Arabia*

Abstract Intercalation reactions can be achieved through ion-exchange, pillaring, and exfoliation–reassembling reactions to explore new intercalation compounds with desired electronic, electrochemical, and optical functions. Such intercalative nanohybrids with lamellar or porous structure have received much attention due to their potential applications such as catalysts, electrodes, selective adsorbents, stabilizing agents, and even drug delivery systems. In this review, we briefly introduce and highlight X-ray diffraction and X-ray absorption spectroscopy studies on the intercalative nanohybrids to understand their intracrystalline and electronic structures along with physicochemical functions.

© 2015 The Authors. Production and hosting by Elsevier B.V. on behalf of King Saud University. This is an open access article under the CC BY-NC-ND license (http://creativecommons.org/licenses/by-nc-nd/4.0/).

* Corresponding author at: Center for Intelligent Nano Bio Materials (CINBM), Department of Chemistry and Nano Science, Ewha Womans University, Seoul 120-750, Republic of Korea.
E-mail address: jhchoy@ewha.ac.kr (J.-H. Choy).
[1] Contributed equally to the work reported.

Contents

1. Introduction

In material chemistry, 'intercalation' denotes a chemical process in which guest species are reversibly inserted into an interlayer space of two-dimensional inorganic hosts to form new heterostructured materials (Park et al., 2013; Choy et al., 1997a; Choy, 2004; Ogawa and Kuroda, 1995; Whittingham and Jacobson, 1982; Bruce and O'Hare, 1997). As widely studied, atoms, molecules, clusters and their charged species, whatever they are inorganic or organic or bio ones, could be intercalated into inorganic lamellar solids, i.e. natural cationic clays, synthetic anionic clays (layered double hydroxides: LDHs), layered metal oxides, layered metal chalcogenides, layered zirconium phosphates and carbonaceous layered compounds (Choy et al., 2007; Oh et al., 2009; Paek et al., 2006a; Kim et al., 2008; Lim et al., 2014; Auerbach et al., 2004; Wang and O'Hare, 2012). Currently those intercalative nanohybrids including inorganic/clay, organic/clay, and biomolecule/-clay nanohybrid materials synthesized through the intercalation reaction have attracted considerable interest due to their wide range of applications for energy, environmental, and medical healthcare industries (Paek et al., 2011; Hitzky et al., 2010; Gunjakar et al., 2014; Oh et al., 2011; Mudhivarthi et al., 2007; Lee et al., 2009; Zeng et al., 2013; Gomes et al., 2013).

In order to develop new nanohybrids for scientific value or practical use, one must understand their crystal structures in the first place. In general, the intercalation compounds based on layered silicates or LDHs could be systematically characterized by X-ray diffraction (XRD) analysis. But if they are not good in crystallinity, due to their porous and/or X-ray amorphous nature, their structural analyses should be done not only by conventional XRD and small angle X-ray scattering but also by X-ray absorption spectroscopy (XAS), nuclear magnetic resonance spectroscopy (NMR), molecular dynamics simulations, and microscopic tools including SEM and TEM (Alvim and Miranda, 2015; Bergaya and Lagaly, 2013; Auerbach et al., 2004; Williams and O'Hare, 2006; Williams et al., 2007; Taviot-Guého et al., 2010).

To characterize layered compounds and their intercalative nanohybrids, the powder XRD is the most common way of solving their structures together with 1-dimensional electron density map calculation, since the well-ordered intercalative nanohybrids show, in general, serially well-ordered *(001)* diffraction peaks corresponding to a basal spacing (*d*) that is increased to higher values upon intercalation. If we could get relatively a large number of *(001)* reflections for the intercalated nanohybrids, one-dimensional (1D) electron density maps along the crystallographic *c*-axis could be achieved *via* Fourier transform analysis. These results can suggest intracrystalline structures such as molecular orientations and arrangements of guest species in the interlayer space.

However, it is not always easy to understand chemical bonding nature and local structure of layered or porous nanohybrids only by conventional powder XRD analysis, since analytically sufficient number of *(001)* reflections is required, but not often observed because of their low dimensionality and poor crystallinity. From these points of view, X-ray absorption near edge structure (XANES) and extended X-ray absorption fine structure (EXAFS) analyses are recommended in order to gain clearer insights on local chemical environments around a specific atom in a molecular scale, such as oxidation states and atomic coordinations (Rehr and Albers, 2000; Lytle, 1999; Wang et al., 2008).

In this review, we will highlight X-ray characterizations of functional intercalative nanohybrids of layered silicates and LDHs reported to date based on not only powder diffraction method with 1D electron density mapping technique but also absorption spectroscopic methods (EXAFS and XANES) to determine the evolution of local coordination environment and electronic structures of guest species and host upon intercalation. Theoretical principles and experimental findings will be discussed not only to simply demonstrate so many examples, but also to help you understand the intercalation reaction mechanisms as well as the chemical bonding natures of intercalative nanohybrids, and how they are correlated with functional applications.
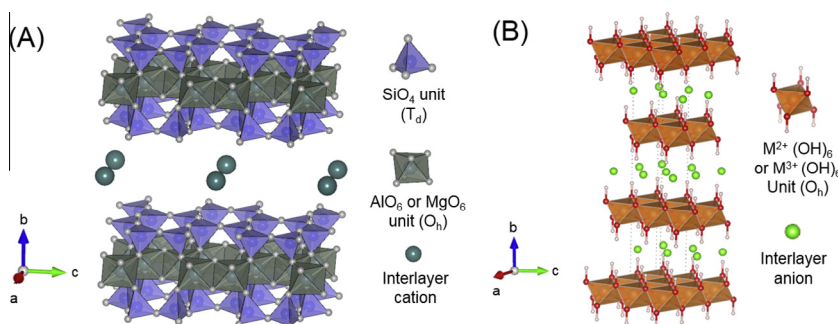
Figure 1 Crystal structures of (A) MMT and (B) LDHs.

2. Structural aspects of lamellar compounds

2.1. Cationic clays: layered silicates

Smectite clays, including montmorillonite (MMT), saponite and hectorite, belong to the 2:1 (ratio of tetrahedral sheet to octahedral sheet) type layered silicates. The smectite is formed structurally by sequential stacking of two-dimensional infinite sheets along the c-axis, where each layer consists of two SiO_4-tetrahedral (T_d) sheets sandwiching a central octahedral (O_h) one of aluminum or magnesium (Fig. 1(A)) (Bergaya and Lagaly, 2013). If Si^{4+} in tetrahedral sheets were substituted isomorphously with lower valent Al^{3+} or Fe^{3+}, and/or Al^{3+} or Mg^{2+} in octahedral sheets were partially substituted also with lower valent Mg^{2+} or Fe^{2+} or with Li^+, a negative layer charge could be generated. Such a negative layer charge can be balanced by interlayer cations such as hydrated Na^+ and Ca^{2+} ions between the silicate layers, those which are readily exchangeable with another cationic species, whatever they are inorganic, organic, or bio-active molecules.

2.2. Anionic clays: layered metal hydroxides

LDHs, known as anionic clays due to their anionic exchange properties, are referred to as hydrotalcite-like materials because the structure and origin of cationic layer are similar to the hydrotalcite mineral found in nature, $Mg_6Al_2(OH)_{16}CO_3 \cdot 4H_2O$. The general formula of LDHs can be described as $[M^{2+}_{1-x}M^{3+}_x(OH)_2]^{x+}(A^{m-})_{x/m} \cdot nH_2O$, where M^{2+} is a divalent metal cation, M^{3+} is a trivalent one, and A^{m-} is the interlayer anion. To describe its crystal structure, it would be better to begin with the structure of brucite, $Mg(OH)_2$, where divalent Mg^{2+} ions are octahedrally coordinated with six hydroxo (OH) ligands to form octahedra, and these octahedra are bound one another by sharing edges to form an infinite sheets. Those sheets are then stacked on the top of each other to build up the layered structure through hydrogen bonding. In the LDH structure, however, divalent metal cations, such as Mg^{2+}, Zn^{2+}, Ni^{2+}, Ca^{2+}, and Fe^{2+}, are partially substituted by higher valent metal cations such as Al^{3+}, Cr^{3+}, Fe^{3+} and Ti^{4+} resulting in a positive layer charge in the lattices. To compensate for the positive layer charge, solvated anionic species are simultaneously intercalated in the interlayer space of LDH lattice, which can be then exchanged with other anionic molecules (Fig. 1(B)) (Rives, 2001).

3. Powder XRD analysis and 1D electron density calculation

3.1. Evaluation of 1D electron density map

XRD is a basic and powerful tool for characterizing the crystal structures of various solids, but if the structural refinement is needed, Rietveld analysis, the whole XRD pattern fitting procedure for structural refinement, has often been made for the polycrystalline samples with good crystallinity (Kim et al., 2001; Choy et al., 1996, 2001a; Young, 1993). In case of layered materials, such as cationic and anionic clays, and their intercalative hybrids, however, it is usual to observe broad and asymmetric X-ray diffraction peaks, due to the lattice strains upon intercalation, such as structural defects and stacking faults (Yang et al., 2007, 2013; Kim et al., 2013). It is, therefore, not that easy to do Rietveld refinement analysis, due to the fact that the X-ray diffraction data collected are often not in good quality, i.e. poor (hkl) reflections from the intercalated hybrids, except a few sharp and strong $(00l)$ peaks. This is probably the reason why only a few papers on Rietveld refinement have been reported so far for the clay hybrids intercalated with small organic and inorganic molecules, such as dimethylsulfoxide (DMSO), Cl^-, and CO^{3-} (Thompson and Cuff, 1985; Thevenot et al., 1989; Costantino et al., 1998; Ennadi et al., 2000).

But if a large number of well developed *(00l)* peaks are available for the intercalative hybrids of layered silicates and LDHs, one can propose the structural conformation, orientation and arrangement of guest molecules in the interlayer space *via* a Fourier transformation of a series of *(00l)* peak intensities, resulting in 1-d electron density map along the c-axis (Whittingham and Jacobson, 1982; Kim et al., 2013; Choy et al., 1997b; Kuks and Huh, 1997; Besserguenev et al., 1997; Vicente et al., 1999; Lavela et al., 1996; Leroux and Taviot-Guého, 2005). The 1D electron density map can be calculated with Eq. (1) using *(00l)* peaks with high periodicity in the XRD patterns for the intercalative nanohybrids (Itoh et al., 2005; Kennard, 1972; Delatorre and de Azevedo, 2001; Ladd and Palmer, 1994).

$$\rho(z) = \sum_{l=-\infty}^{\infty} F(00l) e^{-i\left(\frac{2\pi l z}{c}\right)} \qquad (1)$$

This equation for centrosymmetric structures can be transformed to the following one (Eq. (2)):

$$\rho(z) = 2\sum_{l=0}^{\infty} F(00l) \cos\left(\frac{2\pi l z}{c}\right), \qquad (2)$$

and $F_o(00l) = e^{-i\varphi(l)} \sqrt{|I(00l)|}$

where l, $F_o(00l)$, c, z, $I(00l)$, and $\varphi\ (00l)$ denote the order of $(00l)$ diffraction peak, the observed structure factor, the unit cell parameter of c-axis, the atomic coordinate along the z-axis, the integral intensity of $(00l)$ peak, and the phase, respectively. The functions could be synthesized from $z/c = -1.0$ to 1.0 for the intercalative nanohybrids. In calculation of $F_o(00l)$, the intensity of $(00l)$ reflection peak is corrected with Lorentz-Polarization (LP) factor (Pecharsky and Zavalij, 2005), and the temperature factor and absorption factor could be approximately omitted in Debye–Sherrer method.

$$LP = \frac{1 + \cos^2 2\theta}{\cos\theta \cdot \sin^2\theta}$$

The sign of observed structure factor is obtained from that of the structure factor calculated from the expected structure model. The structure factors corresponding to the expected structure model can also be calculated from atomic scattering factor and position of atoms in that model structure. The structure factor for centrosymmetric materials is calculated using the following equation:

$$F_c(00l) = \sum_{i=0}^{N} f_i \cos(2\pi l z_i),$$

where f_i is the atomic scattering factor for each atom in the unit cell (Kennard, 1972; Delatorre and de Azevedo, 2001). The atomic scattering factors can be obtained from "International Tables for X-ray Crystallography" or other references (Ibers and Hamilton, 1989; Su and Coppens, 1997). The initial position of atoms in host layer can be taken from the crystal structure of the pristine layered materials before intercalation reaction, and the initial interlayer structure model of guest species is set up based on the Patterson diagram and the energy minimized chemical structure. (Lavela et al., 1996; Vicente et al., 1999) Through this process, one can obtain the observed one dimensional electron density (ρ_o), derived from the experimental XRD intensity, and the calculated one (ρ_c), derived from the expected structure model. Finally, we can determine the rational orientation of guest molecules in layered structure by comparing those profiles. The reliability factor (R) can be calculated with the following equation (Uehara et al., 1999; Delatorre and de Azevedo, 2001):

$$R = \frac{(\sum ||F_o(00l)| - |F_c(00l)||)}{\sum |F_o(00l)|}$$

3.2. 1D Electron density map of cationic clays and their intercalative nanohybrids

There have been several reports on 1D electron density mapping for organic-intercalated layered silicates to study the orientation of organic molecules stabilized in the interlayer space (Fujita et al., 1997; Adams et al., 1976; Adams, 1974; Argüelles et al., 2010; Bergaya and Lagaly, 2013). For example, Fujita et al. (1997) studied the interlayer molecular orientation of rhodamine 6G (R6G) in Li-fluortaeniolite, one of the smectite-type clays, by calculating 1-d electron density along z-direction from ten well-ordered $(00l)$ diffraction peaks. Based on the basal spacing of 22 Å, they could propose two possible

orientation models of R6G in the interlayer for the Fourier transformation: one is a vertical model where the longest axis of xanthene ring in R6G is perpendicular to the basal plane of layered silicate, and the other is a parallel model, where that of xanthene ring is parallel to the basal plane of layered silicate. For the parallel model, it was assumed as if R6G molecules were oriented with bilayer stacking arrangement.

In contrast, a perpendicular monolayer orientation could be inferred from the vertical model for the whole range of R6G content in layered silicate. And this vertical model is well consistent with the constant basal spacing for various R6G contents. The R-factor for the vertical model was fitted to an excellent value of 1.2%. On the other hand, the R-factor was $\sim$20% for the parallel models. As shown in Fig. 2, the 1D electron density profile and difference Fourier synthesis are represented together with the proposed vertical model including the positional parameters for R6G intercalated in layered silicate. Based on this 1D electron density mapping, it was concluded that R6G was intercalated with a monolayer perpendicular orientation to the ab plane of host layer, and the positively charged N atoms of R6G were bonded to the negatively charged silicates by strong electrostatic interactions.

A similar study on 1-d electron density mapping was also made for an inorganic guest intercalated vermiculite by Uehara et al. (1999). They were successful in intercalating the $Ni(OH)_2$ sheets into layered silicates and suggested a monolayer orientation of $Ni(OH)_2$ simply by comparing the calculated and observed electron density maps with a reasonable R value of 0.10. As an example of organic guest-clay host hybrid, Adams (1974) and Adams et al. (1976) reported that an organic molecule like tetrahydrofuran (THF) and tetrahydropyran could be intercalated into MMTs containing various cations such as NH^{4+}, Na^+, Sr^{2+}, Co^{2+}, Ni^{2+}, and Cu^{2+}. From the 1D electron density calculation, it was concluded that THF molecules were ordered perpendicularly to the silicate layers. Kanamaru and Vand (1970) also suggested a parallel bilayer orientation of 6-amino hexanoic acid in the vermiculite lattice by plotting the 1D electron density map. Argüelles et al. (2010) also suggested the positions for the interstitial water molecules in vermiculite through the 1D electron density profile analysis.

3.3. 1D electron density map of anionic clays and their intercalative nanohybrids

There have been a number of reports on 1D electron density calculations of LDHs intercalated with organic molecules (Kuks and Huh, 1997; Illaik et al., 2008; Huang et al., 2012; Marangoni et al., 2008; Cunha et al., 2012; Itoh et al., 2005). Recently, Kim et al. (2013) also reported flurbiprofen (FB) intercalated Zn_2Al-LDH as a new transdermal drug delivery system with its 1D electron density calculation result to understand the interlayer arrangement of FB drug molecules in between the layered lattice (see Fig. 3). The integral intensities of six well-developed $(00l)$ peaks were used for Fourier transformation. The positional parameters of Zn, Al, and OH in the LDH layer were obtained from the crystal structure of Zn_2Al–CO_3 LDH. And they found that the rational interlayer structure of FB molecules was an interdigitated bilayer one oriented with a tilt angle of $\sim$21° by comparing the calculated and observed electron density profiles based on different interlayer
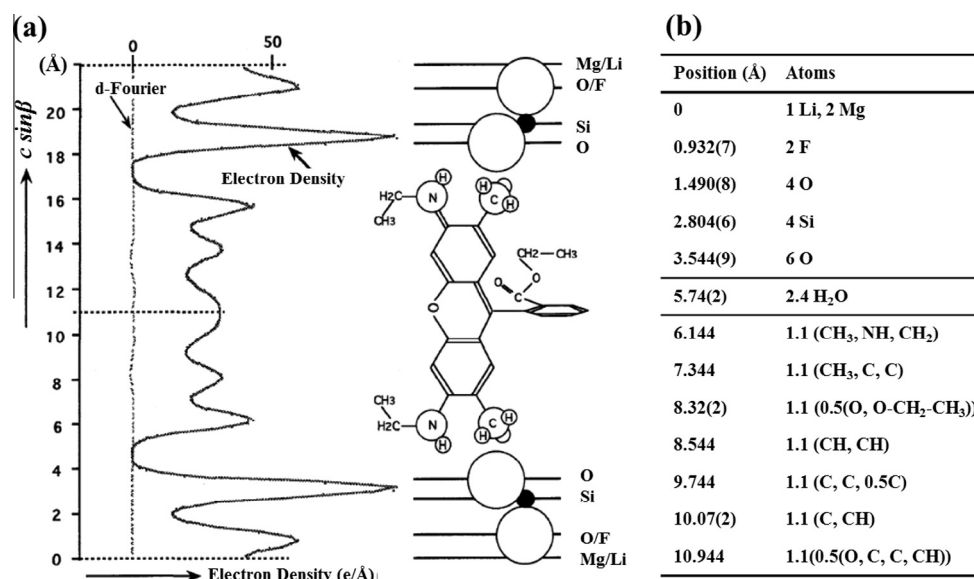
Figure 2 (a) The orientation of rhodamine 6G (R6G) in layered silicates and its 1D electron density profile along *z*-direction, and (b) positional parameters of R6G intercalated layered silicates hybrid. Reprinted from reference Fujita et al. (1997). Copyright 1997 The Clay Minerals Society.
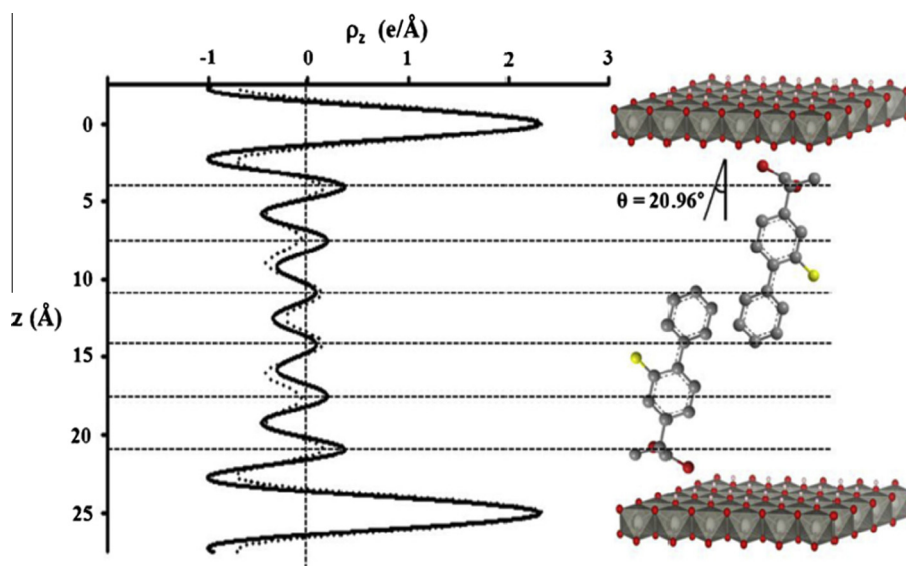

Figure 3 1D electron density profiles along *z*-direction for the flurbiprofen intercalated Zn_2Al-LDH and its corresponding structural model, where the solid and dashed lines indicate the observed and calculated electron density profile, respectively. Reprinted from reference Kim et al. (2013). Copyright 2013 Elsevier Ltd.

orientation models with a tilting angle of interdigitated bilayer from 0° to 31.6°. A strong peak at the *z*-parameter of 0 Å in 1D electron density map corresponds to Zn and Al in the LDH layer, and six additional peaks with lower electron densities could be attributed to the intercalated FB and water molecules in the interlayer.

Káfuňková et al. (2010) reported 1-d electron density map calculation to understand the intracrystalline structure of porphyrin molecules stabilized in the ZnAl-LDH lattice and MgAl LDH one. According to the powder XRD study, the peak positions and their intensities and the refined unit cell parameters were obtained by profile refinement analysis. From seven

well-ordered *(00l)* peaks, the interlayer structure of porphyrin molecules projected on the *z*-direction was determined as the perpendicularly oriented with respect to the basal plane of LDH, where the sulfonate groups gave rise to the second electron density maxima at the outer parts of interlayer space due to the hydrogen bonding between the sulfonate groups in porphyrin molecules and OH groups on LDH layers along with electrostatic interactions induced by perpendicularly oriented porphyrin anions against the LDH surface. As another example, an interlayer orientation of organic molecule such as 4[12-(methacryloylamino) dodecanoylamino] benzenesulfonate acid (MADABS), intercalated in Zn_2Al-LDH was demonstrated by

Illaik et al. (2008) through 1D electron density profile calculation. Though the molecular structure of MADABS is rather flexible and complicated, their interlayer assembling arrangement was rather well determined as an interdigitated bilayer one with a tilting angle of ~20°. As mentioned above, 1D electron density mapping is a good analytical tool to understand the interlayer structure of guest molecular assembly simply by performing the powder XRD analysis.

3.4. X-ray diffraction profile simulation for interstratified nanohybrids

In general, the intensity of (00l) X-ray diffraction peaks for intercalative layered materials such as layered silicates and LDHs exponentially decreases with an increase of l, due to the Lorentz polarization effect (Pecharsky and Zavalij, 2005). However, it is often found that the intensity of (001) is weaker than that of (002) in the range of low 2θ angles in case of layered compounds with staging structure, that is an interstratified structure, where two layered units or more are arranged regularly or irregularly along the c-axis direction (Tateyama et al., 1998; Yang et al., 2001; Claret et al., 2004; McCarty et al., 2008; Williams et al., 2004; Taviot-Guého et al., 2010). Such an interstratified structure could be confirmed by comparing observed XRD profiles and theoretical ones calculated from an expected structural model based on Kakinoki and Komura's equation (Yang et al., 2001; Kakinoki and Komura, 1965; Sato, 1987). The integrated intensity of theoretical XRD profile for an interstratified layered material consisted of N layers and n types of layers can be calculated by using the following equation:

$$I = N \, \mathrm{Spur}(VF) + \sum_{n=1}^{N-1} (N-n)\mathrm{Spur}(VF(\Phi P)^n) + conj., \quad (3)$$

where Spur and *conj.* stand for the summation of diagonal elements of square matrix, and the complex conjugate of foregoing terms, respectively. V is the matrix of structure factors for each layer, F is the matrix of existing probability, P is the matrix of transition probability from one layer to the next, and Φ is the matrix of phase factors. The intensity is finally obtained by multiplying by Lorentz polarization factor. For the interstratified layered nanohybrid composed of two kinds of layers (1st layer and 2nd layer), the matrixes of V, F, P and Φ, and the relationships between proportions of the different kinds of layers and probabilities are given by the following:

$$W_1 + W_2 = 1$$

$$P_{11} + P_{12} = 1$$

$$P_{21} + P_{22} = 1$$

$$W_1 \cdot P_{12} = W_2 \cdot P_{21}$$

$$V = \begin{bmatrix} V_1 * V_1 & V_1 * V_2 \\ V_2 * V_1 & V_2 * V_2 \end{bmatrix}, \quad F = \begin{bmatrix} W_1 & 0 \\ 0 & W_2 \end{bmatrix}$$

$$P = \begin{bmatrix} P_{11} & P_{12} \\ P_{21} & P_{22} \end{bmatrix}, \quad \Phi = \begin{bmatrix} \exp(-\Psi_1) & 0 \\ 0 & \exp(-\Psi_2) \end{bmatrix},$$

where W_1, W_2, V_1, V_2 are the existing probability and the matrix of structure factor of 1st layer and 2nd layer, respectively.

The independent values of these parameters are W_1 and P_{12}, because the other parameters can be evaluated from W_1 and P_{12} using the relationship equations. From the relationships and the equations on intensity, one can simulate the XRD profiles for a structural model expected from an interstratified layered nanohybrid.

Yang et al. (2001) reported one example of n-alkylammonium intercalated interstratified layered silicates. Such an interstratified layered structure could be originated from the layer by layer heterogeneity of layer charge density of fluorine mica. Thus, the intercalation of n-alkylammoniums with C_{10}, C_{12}, and C_{18} into the fluorine mica resulted in the interstratified layered hybrid between parallel monolayer and bilayer (I_{MB}) or parallel bilayer and pseudotriple layer structures (I_{BT}) in mica layers. As well demonstrated, they could obtain better information on the interstratified structure than the previous, such as the probability of existing layers and the probability of stacking sequence of composed layers, by simulating the observed XRD profiles for two different types of interstratified structures with the XRD intensity calculation equation proposed by Kakinoki and Komura (1965).

The expected structural models, the observed XRD patterns, and the best fitted calculated XRD patterns are shown in Fig. 4. The observed XRD profile of C_{10}–M (n-decylammonium intercalated fluorine mica) showed an interstratified structure composed of parallel monolayers and parallel bilayers, which was consistent with the calculated one. By fitting the parameters for this simulated XRD profile, the existing probabilities of the monolayers (W_M) and bilayers (W_B) were evaluated to be 0.55 and 0.45, respectively, and then the transition probabilities were determined to be $P_{MB} = 0.81$ and $P_{BM} = 0.99$. For the C_{18}–M (n-octadecylammonium intercalated fluorine mica), however, the interstratified structure was assumed to be composed of parallel bilayers and parallel pseudotriple layers, the simulation parameters, such as the existing probabilities and the transition probabilities, were determined as $W_B = 0.5$, $W_T = 0.5$, $P_{BT} = 0.99$, and $P_{TB} = 0.99$, respectively. According to the XRD simulation results for those interstratified alkylammonium-fluorine mica hybrids, the layer charge density profile along the c-direction in Na^+ fluorine mica was determined to be not homogeneous, but regularly repeated layer by layer sequentially with higher charge density and lower charge density.

Plançon and Drits (1999) also demonstrated the interesting XRD patterns for a mixed-layer mineral, illite–smectite, and a more complex mixed-layer mineral, illite–smectite–vermiculite, in which smectite was swelled with ethylene glycol. From the XRD simulation, they were able to collect the data on the number of stacked layers and its distribution, and the probability of stacking sequence. All those examples indicated that the XRD simulation method could be a useful tool to understand the crystal structure of mixed layer compounds.

Recently, time-resolved in situ energy dispersive X-ray diffraction (EDXRD) experiment by using synchrotron X-ray has been developed. (Fogg et al., 1998; Taviot-Guého et al., 2010) This method is very useful for the investigation of mechanism and kinetics for the intercalation reaction, because all of the intercalation reaction could be simultaneously observed as soon as the guest solution is added into
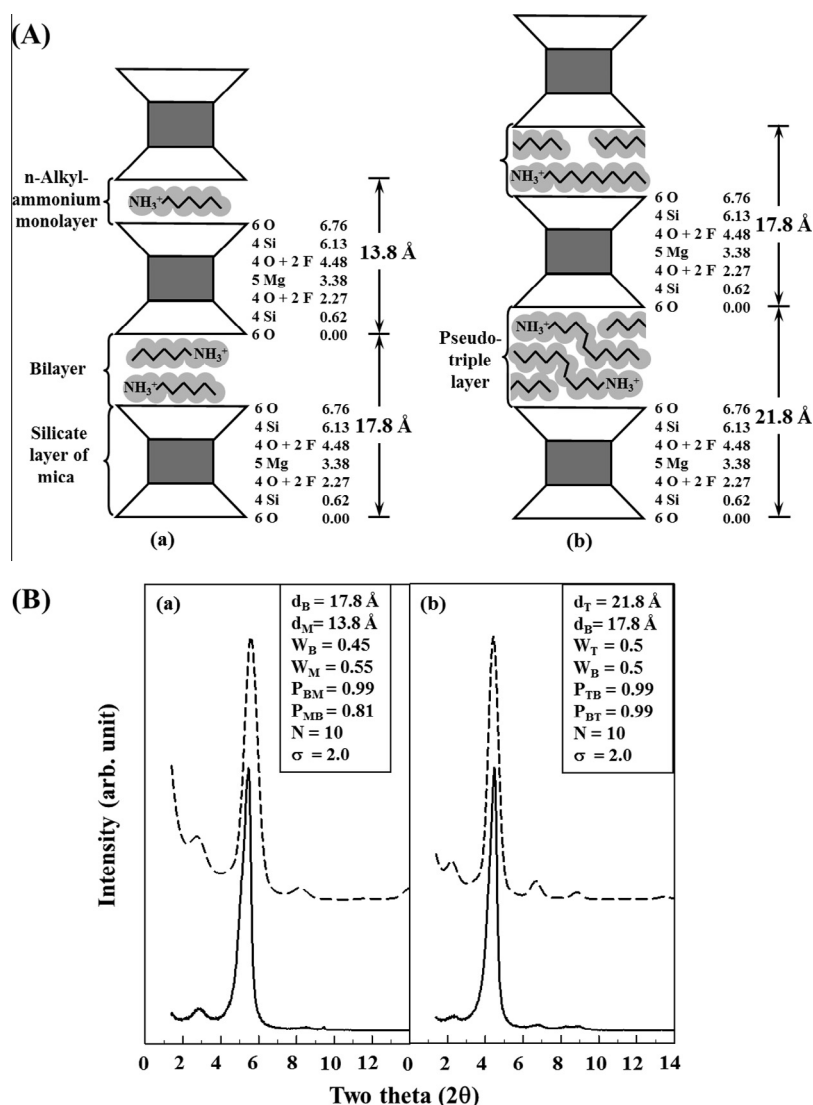
Figure 4 (A) Structural model used in the simulation of XRD profiles for interstratified structures. (a) Between parallel monolayer and bilayer (I_{MB}), and (b) between parallel bilayer and pseudotriple layer (I_{BT}), and (B) the observed (solid line) and calculated (dashed line) powder X-ray diffraction profiles for the interstratified samples; (a) C_{10}–M (I_{MB}) and (b) C_{18}–M (I_{BT}). The best fitted simulation parameters are summarized in the insets. Reprinted from reference Yang et al. (2001). Copyright 2001 The Royal Society of Chemistry.

the host suspension. Taviot-Guého et al. (2010) reported the second staging phenomena (interstratified structure) during the intercalation of tartrate into Zn_2Cr-Cl LDH. And Williams et al. (2004) could also demonstrate the staging structure during the phosphonic acid interaction into $LiAl_2$-Cl LDH via this time-resolved XRD analysis.

4. XAS analyses for the advanced functional materials with low crystallinity

4.1. Principles of XANES and EXAFS analyses

The X-ray absorption spectroscopy (XAS) is one of the most precise measurement techniques to understand the local structure around a specific atom in materials based on X-ray absorption coefficient as a function of incident X-rays in energy range (Rehr and Albers, 2000; Lytle, 1999). As well documented, X-ray absorption near edge structure (XANES)

is a sensitive tool to probe oxidation state and coordination number of an absorbing atom of interest. The electronic and geometric structures of an atom can be determined because the spectral features in the region from pre-edge to ~40 eV are originated from the transitions of core level electrons to unoccupied states above Fermi level ($1s \rightarrow np$ for K-edge, $2s \rightarrow np$ for L_I-edge, $2p_{1/2} \rightarrow ns$ and nd for L_{II}-edge, and $2p_{3/2} \rightarrow ns$ and nd for L_{III}-edge). From extended X-ray absorption fine structure (EXAFS) analysis, however, one can assess quantitative local environments around a specific atom: the type and the number of nearest-neighboring atoms around an atom of interest as well as the average interatomic distances through a radial distribution function.

XANES and EXAFS data analyses from experimental spectra can be performed by standard procedures (Choy et al., 1995, 1997c, 2002, 2003). X-ray absorption spectroscopic measurement is normally carried out with synchrotron radiation by using the EXAFS facilities. If the X-ray absorption is plotted

as a function of energy (eV), the XAS spectrum is divided into XANES region within ca. 50 eV of the edge and EXAFS region for the several hundred to > 1000 eV above the edge. At first, the inherent background is removed from the entire spectrum by fitting a polynomial to pre-edge region and subtracting the fitted background. The absorbance, $\mu(E)$, is then normalized by adjusting an edge jump of unity for comparing the XANES features with one another. The absorption spectrum for the isolated atom, $\mu_0(E)$, is approximated by a cubic spline-function. The EXAFS function, $\chi(E)$, is then expressed as $\chi(E) = \{\mu(E) - \mu_0(E)\}/\mu_0(E)$. Further analysis is performed in a k space, where the photoelectron wave vector k is defined as $k = \{(8\pi^2 m_e/h^2)(E - E_0)\}^{1/2}$, where m_e is the electron mass, h is Planck constant, E is the photon energy, and E_0 is the threshold energy of photoelectron at $k = 0$. The resulting EXAFS spectra are k^3-weighted to compensate for the attenuation of EXAFS amplitude at high k, and then Fourier-transformed (FT) in the range of $\sim 2\,\text{Å}^{-1} \leqslant k \leqslant \sim 13\,\text{Å}^{-1}$ with

a Hanning apodization function of $dk = 0.5\,\text{Å}^{-1}$. To determine the structural parameters, a nonlinear least-squares curve fitting is performed in the R space of the FT, using the UWXAFS2 code (Newville et al., 1993), Athena, MAX (Multiplatform Applications for XAFS), etc. based on the following EXAFS formula:

$$\chi(k) = -S_0^2 \frac{N_i}{k R_i^2} F_i(k) \exp\{-2\sigma_i^2 k^2\} \exp\left\{-\frac{2R_i}{\lambda(k)}\right\}$$
$$\times \sin\{2k R_i + \phi_i(k)\} \qquad (4)$$

The backscattering amplitude, $F_i(k)$, the total phase shift, $\phi_i(k)$, and the photoelectron mean free path, $\lambda(k)$, have been theoretically calculated for all scattering paths by a curved wave *ab initio* EXAFS code FEFF (Sham, 1986; Rehr et al., 2010; Ankudinov et al., 1998; O'day et al., 1994), which have been recently developed to the FEFF9.6 code and is now available at http://feffproject.org/feffproject-feff.html. In the course
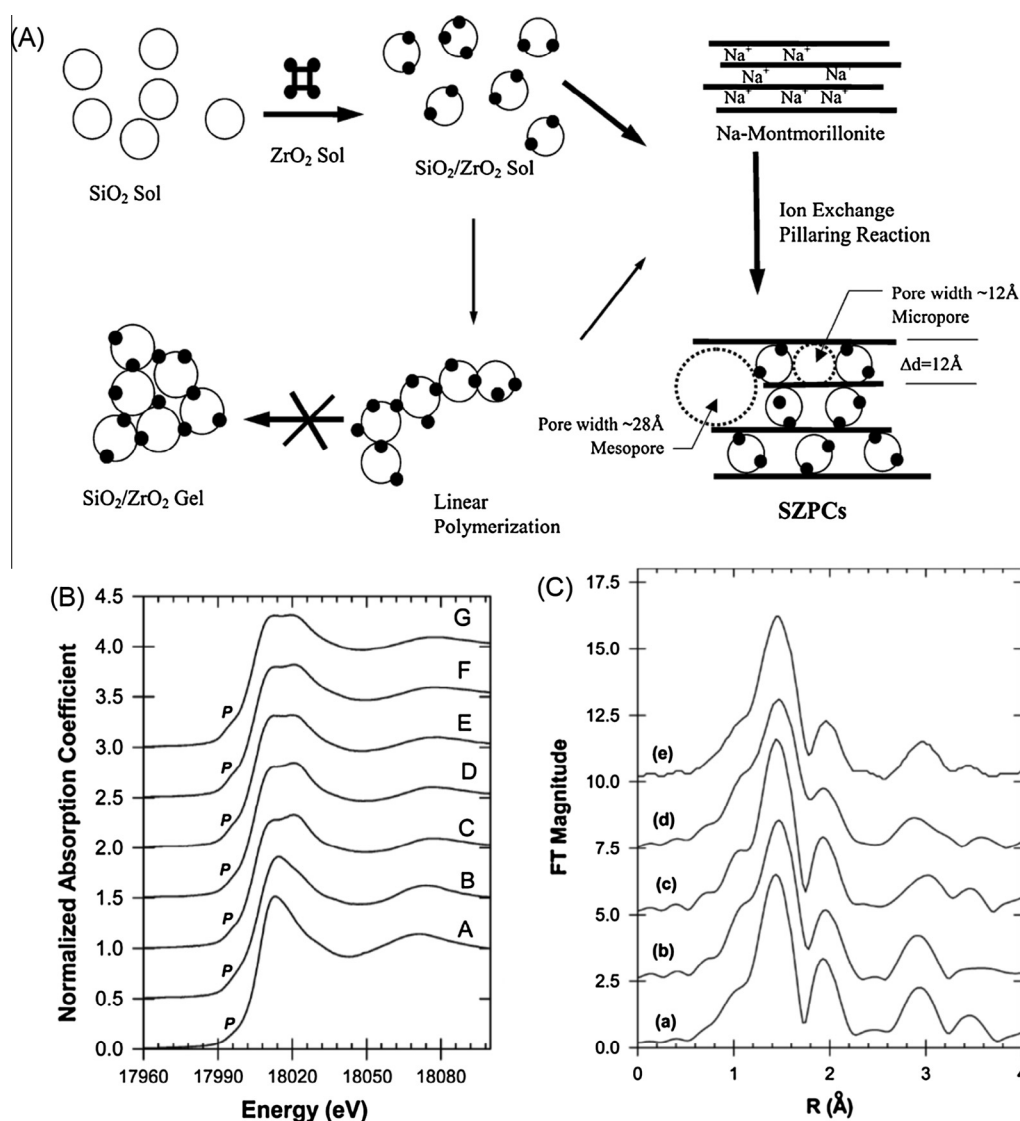

Figure 5 (A) Schematic illustration of the formation mechanism of ZrO_2/SiO_2-pillared MMT, (B) XANES spectra for ZrO_2/SiO_2-pillared MMT at different calcination temperatures and reference compounds: (a) $ZrOCl_2 \cdot 8H_2O$, (b) ZrO_2, (c) wet, (d) 80 °C, (e) 300 °C, (f) 400 °C, and (g) 500 °C (*P*: pre-edge peak), (C) Fourier transforms of the EXAFS spectra of the ZrO_2/SiO_2-pillared MMT: (a) wet, (b) 80 °C, (c) 300 °C, (d) 400 °C, and (e) 500 °C. Reprinted from reference Choy et al. (2003). Copyright 2003 The Royal Society of Chemistry.

of nonlinear least-squares curve fitting procedure between experimental spectrum and theoretical one for the inverse Fourier transformed $k^3\chi(k)$ of the first shell in FT with the aid of Eq. (4), the optimized structural parameters including bond distance (R_i), Debye–Waller factor (σ_i^2), coordination number (N_i), and threshold energy difference (ΔE_0) are determined. The amplitude reduction factor (S_0^2) for interatomic bonds is set equal to 0.9 in the entire course of fitting procedure (Rehr et al., 1991; Mustre de Leon et al., 1991; O'Day et al., 1994). The term of $\exp\{-2R_i/\lambda(k)\}$ represents the inelastic losses in scattering process due to neighboring atoms and medium inbetween, while $\exp\{-2\sigma_i^2/k^2\}$ represents the effects of thermal vibration and static disorder. All of software for XAS data treatment based on the EXAFS formula is available at http://xafs.org/Software.

4.2. XAS analysis for cationic clays and their nanohybrids

There have been many reports on layered or porous nanohybrids based on layered silicates intercalated with organic molecules, polyoxocations, polyoxyhydroxy cations, metal complexes, and metal oxides (Bornholdt et al., 1991; Brendlé et al., 1997; Kawabata et al., 2005; Han et al., 1997, 1999; Han and Choy, 1998; Choy et al., 1998a, 1998b, 2001b, 2001c; Lee et al., 2005; Malferrari et al., 2008; Park et al., 2006). Among them, pillar-clays (PILCs) have attracted great attentions because of their controllable pore dimensions with large surface area and high thermal stability. These PILCs have been considered as functional materials such as catalysts, supports, molecular sieves, selective adsorbents, separating membranes, and sensor materials in clean energy and environmental applications (Choy et al., 2002, 2003; Paek et al., 2006b; Hur et al., 2006; Jung et al., 2007; Kamada et al., 2012; Carvalho et al., 2013; Yang et al., 2011, 2015).

In particular, positively charged metal oxide particles, such as CoO/SiO_2, Cr_2O_3, Fe_2O_3, ZrO_2, TiO_2, ZnO, NiO, and CeO_2, have been successfully intercalated and pillared in between the silicate lattice through the ion-exchange process by the electrostatic interaction in the beginning and eventually

covalent bonding upon heat treatment, resulting in porous pillared structure. Such sol particles-pillared clays were determined to be quite porous with large surface area of 500–900 m^2/g with micro–meso pores, and thermally very stable up to 800 °C, and fairly interesting in terms of various physicochemical properties depending on the type of silicate layers and pillaring agents (Yamanaka et al., 1992; Takahama et al., 1992; Choy et al., 1998c). It has been also found that electronic configuration, mobility, and orientation of pillared species could be influenced by layer charge density and its distribution of silicate lattice. Therefore some attempts have been made not only to characterize electronic structures and coordination environments of transition metal elements within the pillars of layered silicates, but also to understand intercalation mechanism during ion-exchange and post-calcination reactions (Choy et al., 1998c, 2003).

The intracrystalline and electronic structures of metal oxides intercalated and pillared in clay have been studied by XAS analysis. According to the EXAFS study for chromia-pillared clay obtained with oligomeric chromium species like a $[Cr_2(OH)_2(H_2O)_8]^{4+}$, it was found that the cis-linked octahedral Cr^{III} units in aqueous solution were retained upon intercalation, but partially oxidized to the mixed-valent Cr^{III}/Cr^{VI} units after calcination (Bornholdt et al., 1991). However, in the case of microporous chromia-pillared clay prepared by ion-exchange reaction between Na$^+$-MMT and trimeric chromium oxyformate ion $(Cr_3O(HCO_2)_6(H_2O)_3^+)$, the trivalent chromium ion remained unchanged without any oxidation (Choy et al., 1998b). Upon heat treatment, intercalated chromium molecular clusters turned out to be chromium oxide with three different Cr–Cr bond lengths, 2.64, 2.98, and 3.77 Å, corresponding to Cr–Cr distances between face-, edge-, and corner-shared CrO$_6$ octahedra, respectively, similar to Cr_2O_3.

Choy et al. (2003) investigated the changes in local structure of a pillared clay, ZrO$_2$/SiO$_2$-pillared MMT, with a specific surface area of 358 m^2/g and an average micropore size of 12 Å, which was a new mixed, pillared and porous nanohybrid. From the XANES spectra, it was found that the Zr atom was
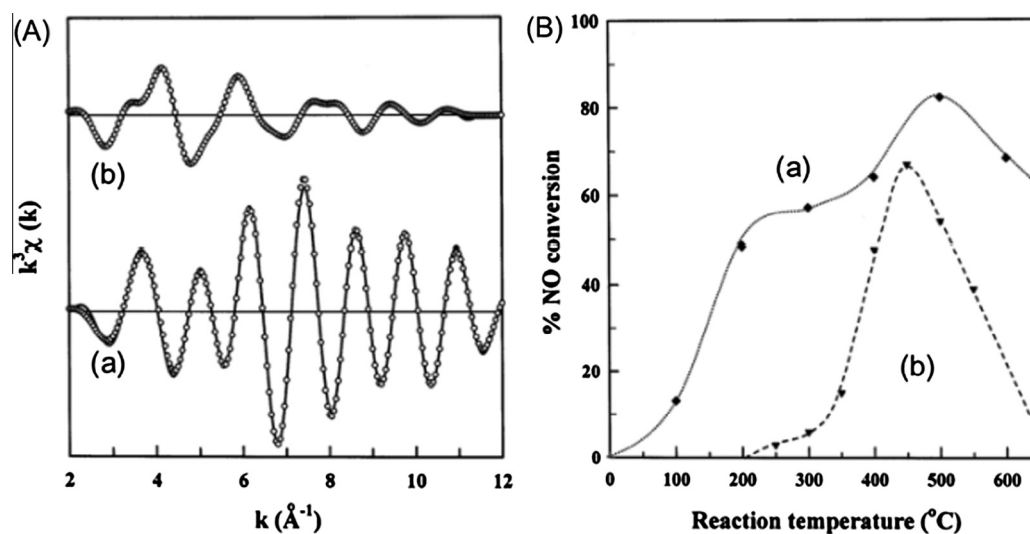

Figure 6   (A) Comparison EXFAS spectra between the experimental (solid line) and the theoretical (symbol) inverse Fourier transforms of the (a) CoO and (b) CoO$_x$/SiO$_2$-pillared MMT. (B) Selective de-NO$_x$ activity of the (a) CoO$_x$/SiO$_2$-pillared MMT and (b) Co ion-exchanged zeolite 5. Reprinted from reference Choy et al. (2002). Copyright 2002 American Chemical Society.
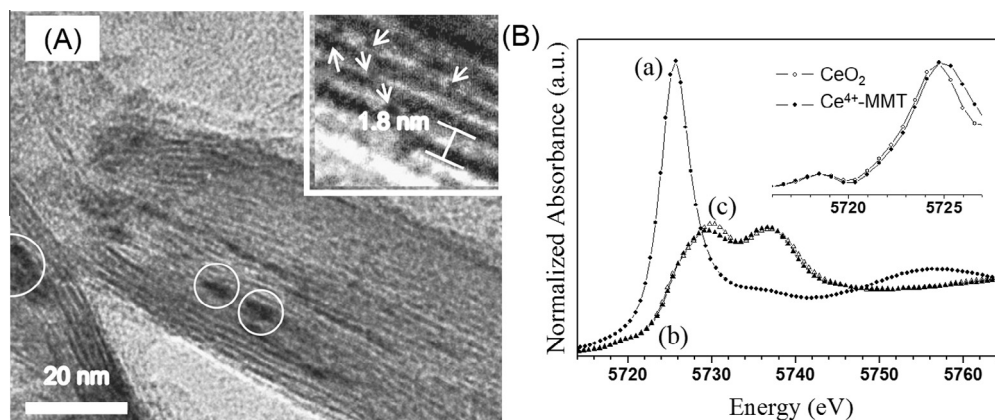
Figure 7 (A) Cross-sectional TEM images of the CeO$_2$-layered MMT. (B) Ce L$_{III}$-edge XANES spectra of the (a) Ce^{3+}-MMT, (b) Ce^{4+}-MMT, and (c) standard CeO$_2$ (inset: first differentiation curves of (b) and (c)). Reprinted from reference Kamada et al. (2012). Copyright 2012 Elsevier Ltd.

stabilized in a distorted octahedral site along with two different distances (2.0 Å and 2.2 Å) and the Zr–O bond length was found to be decreased upon calcination at 300 °C. The average value of Zr–O bond length was ~2.1 Å, consistent with the sum of the ionic radii of Zr^{4+} (0.72 Å) with O^{2-} (1.40 Å) ligand in an octahedron. According to the EXAFS analysis, it was also found that the ZrO$_2$ sols were immobilized on the surface of SiO$_2$ pillars rather than in the bulk network. Based on the XAS results above (Fig. 5), they were able to propose a mechanism of intercalation and consequent pillaring reaction. In the beginning of reaction, the positively-charged tetrameric [Zr$_4$(OH)$_{8+x}$(OH$_2$)$_{16-x}$]$^{(8-x)+}$ ions were adsorbed on the surface of negatively-charged SiO$_2$ nano-sol particles, in which the [Zr–O–Si] linkage was formed along with bond dissociation of the [Zr–O–Zr] framework. In that way, the positively charged ZrO$_2$/SiO$_2$ nano-sols could be intercalated into silicate layers through the electrostatic interaction. At this stage, no further [Zr–O–Si] linkages would be formed in the interlayer of clay, and finally those nano-sol particles were transformed into nanometer-sized oxide pillars upon calcination. Otherwise the sol–gel transformation may occur in a solution, due to the condensation between Zr^{4+} ions and silanol groups on SiO$_2$ in the absence of layered silicates.

A CoO$_x$/SiO$_2$-pillared MMT nanohybrid has been also reported for NO$_x$ conversion (Choy et al., 2002). The CoO$_x$/SiO$_2$-pillared MMT was synthesized by hydrolysis and subsequent condensation of tetraethyl orthosilicate with Co^{2+} ions within the interlayer of alkylammonium-intercalated MMT. Thus prepared nanohybrid showed a high BET specific surface area (S_{BET} = ~570 m^2/g) and a pore volume (V = ~0.65 mL/g). According to the XANES analysis, the pre-edge feature for the Co species in MMT was found to be almost the same with that of CoO, indicating that any oxidative impurity, corresponding to the trivalent Co$_3$O$_4$, was formed on the way of intercalation reaction. From the EXAFS studies, they could obtain the following fitting results under an assumption that two different oxygen shells were in the first neighbor (Fig. 6(A)): two oxygen atoms from the terminal hydroxyl groups on micropores were bound to the Co atom with an average bond distance of 1.98 Å, whereas three or four oxygens from pillars were coordinated to the Co atom with a slightly longer bond distance (2.13 Å). Since the
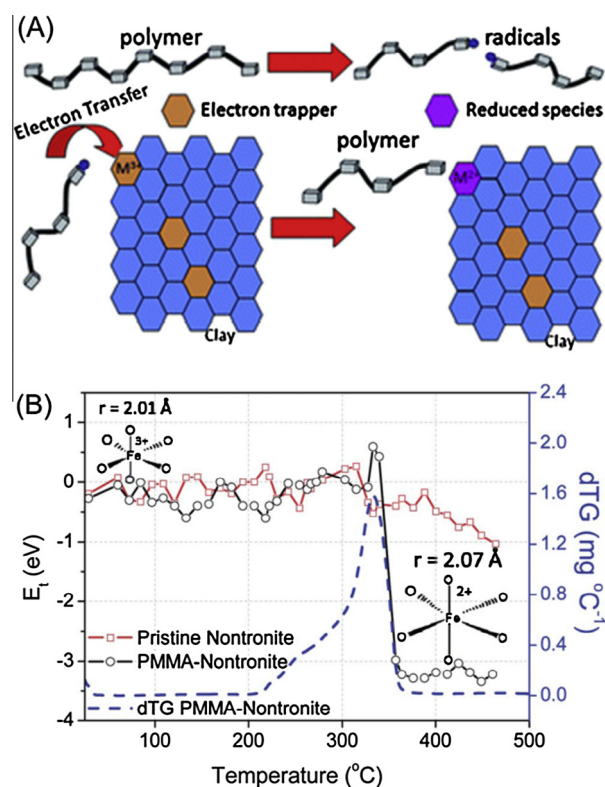

Figure 8 (A) Schematic illustration of radical-trapping flame-retardant mechanism of polymer–clay nanocomposites. (B) Evolution of the threshold energy (E_t) as a function of temperature and dTG curve of the PMMA–Nontronite. Reprinted from reference Carvalho et al. (2013). Copyright 2013 The Royal Society of Chemistry.

CoO clusters were quite homogeneously distributed on the surfaces of SiO$_2$ pillars, the porous CoO$_x$/SiO$_2$-pillared MMT could give rise to a higher catalytic activity for selective NO reduction than the other Co-bearing catalysts (Fig. 6(B)): the conversion rate was 50% even at a temperature as low as 200 °C and reached to 85% at 550 °C.
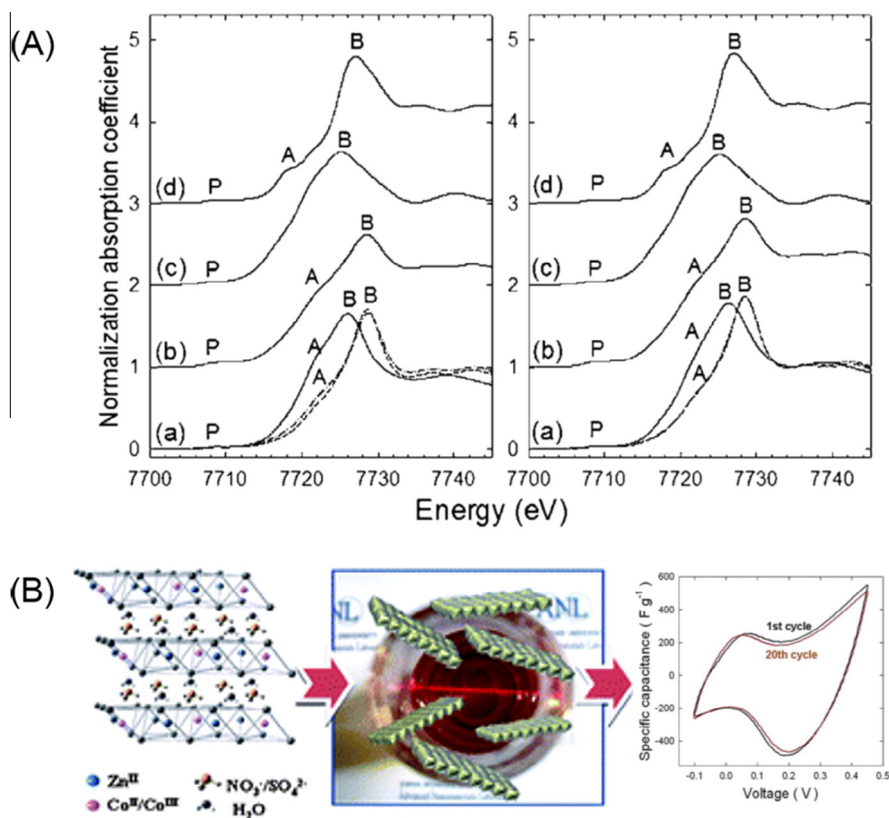
Figure 9   (A) Co K-edge XANES spectra (left) and Zn K-edge XANES spectra (right) of (a) the as-prepared Zn–Co LDHs and their calcined derivatives at 600 and 800 °C, and the reference structures of (b) $ZnCo_2O_4$, (c) CoO, and (d) $LiCoO_2$ (P: pre-edge peak, A and B: characteristic main-edge peaks). (B) A structure model with photograph of the colloidal suspension of the Zn–Co LDH nanosheets, and CV curves of the film restacked with Zn–Co LDH nanosheets. Reprinted from reference Woo et al. (2011b). Copyright 2011 The Royal Society of Chemistry.

Recently, a CeO_2-pillared MMT nanohybrid was prepared by ion-exchange reaction, where hydrated interlayer Na^+ ions were exchanged with Ce^{4+} ones in aqueous solution. In this case, $(NH_4)_2Ce(NO_3)_6$ was dissolved in water in order to dissociate into NH^{4+} and $Ce(NO_3)_6^{2-}$ in solution, since the formed Ce-containing molecular anions could simultaneously decompose into positively-charged cerium hydroxide ion, $Ce(OH)_x^{(4-x)}$, due to the self-hydrolysis reaction with water molecules (Kamada et al., 2012). From the cross-sectional TEM image (Fig. 7(A)), they found that the CeO_2 nanoparticles with a size of 5–10 nm in diameter were immobilized in the MMT layer with the formation of lattice defects.

The electronic structure and local atomic environment of CeO_2-pillared MMT were also investigated at the Ce L_{III}-edge XANES (Fig. 7(B)). A single peak around 5727 eV was observed in Ce^{3+}-MMT due to the $2p \to 4f^1$ 5d dipole-allowed transition. A remarkable splitting at 5730 and 5737 eV and a shoulder peak around 5720 eV were observed in the absorption edge for both Ce^{4+}-MMT and standard bulk CeO_2. These results were attributed to the $2p \to 4f^0$ 5d in tetravalent electronic configuration of Ce and the transitions to the bottom of conduction band, respectively. Moreover, the CeO_2 in Ce^{4+}-MMT showed direct band gap energy of 3.0 eV indicating that the absorption edge was slightly red-shift compared to the CeO_2 bulk (3.1 eV). On the basis of those results, they concluded that tetravalent Ce ions were dominated in Ce^{4+}-MMT, and therefore, such an inorganic–inorganic nanohybrid could be applicable as a useful UV screening agent.

More recently, Carvalho et al. (2013) demonstrated, for the first time, the flame-retardant mechanism for a polymer-layered silicate nanohybrid through *in-situ* time-resolved XAS analysis. As a chemical effect of layered clay on the improvement of thermal stability of polymer composites, the so-called "radical trapping," was observed with *in-situ* XAS analysis. For example, they prepared the poly(methylmethacrylate) (PMMA)-clay nanohybrids based on three kinds of natural MMT clays: Arizona MMT, Wyoming MMT, and Nontronite. The content of structural Fe ions in each clay was 0.32%, 1.02%, and 8.10%, respectively. By *in-situ* time-resolved XAS measurements, it was clearly demonstrated that Fe^{3+} ions in all clays was reduced to Fe^{2+} through electron transfer from the radicals, which were formed by thermal decomposition of PMMA polymer, to the clay lattice (Fig. 8(A)).

From the comparative study on the absorption edge energy as a function of temperature overlapped with dTG curve (Fig. 8(B)), it was found that the absorption edge energy for the PMMA–Nontronite was red-shift about 3.5 eV compared to that for the pristine Nontronite at 450 °C, due to the fact that the Fe^{3+} ions in the clay lattice were reduced to the Fe^{2+} ones, which was consistent with an increase in (Fe–O)
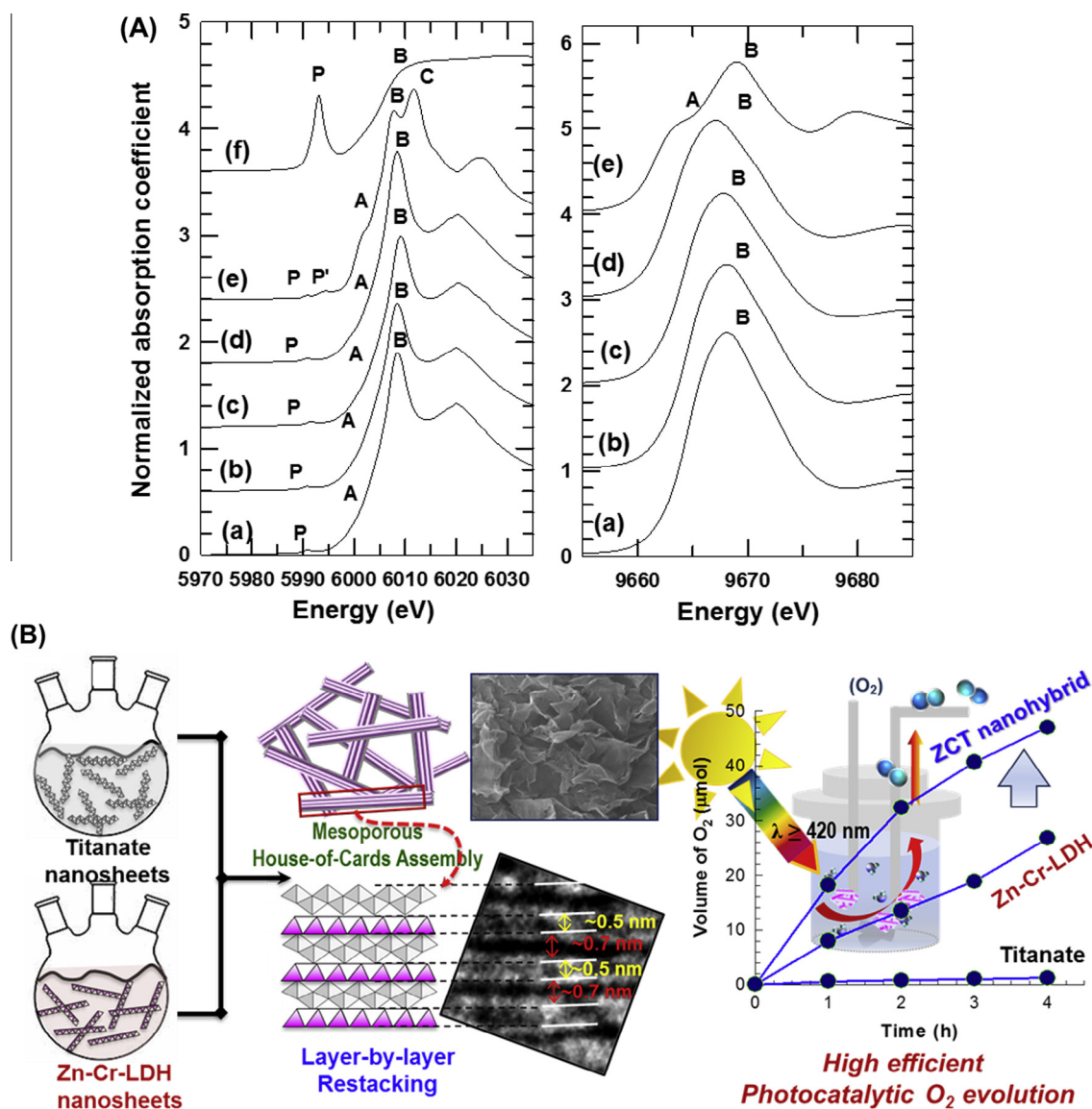
Figure 10 (A) Cr K-edge (left) and Zn K-edge (right) XANES spectra of (a) ZCT-1 (the ratios of layered titanate/layered ZnCr LDH with 0.91), (b) ZCT-2 (the ratios of layered titanate/layered ZnCr LDH with 1.16), and (c) ZCT-3 (the ratios of layered titanate/layered ZnCr LDH with 1.46), (d) the protonated layered titanate/ZnCr–LDH/ZnCr–LDH, (e) anatase $TiO_2/Cr_2O_3/ZnO$ and (f) rutile TiO_2/ CrO_3. (B) A structural model with SEM/TEM images and time-dependent photo-production of oxygen gas under visible light illumination ($\lambda > 420$ nm) for ZCT-1 and pristine Zn–Cr LDH. Reprinted from reference Gunjakar et al. (2011). Copyright 2011 American Chemical Society.

bond distance from 2.01 to 2.07 Å. It is, therefore, concluded that the clay could play a role not only as an electron acceptor but also as a radical trapper, and as a consequence, significantly retard the polymer decomposition and eventually improve the thermal stability of polymer matrix.

4.3. XAS analysis for anionic clays and their nanohybrids

LDHs and their intercalative nanohybrids are of increasing interest due to their catalytic, photoactive, and electroactive applications (Intissar et al., 2003; Yu et al., 2015; Woo et al., 2011a, 2011b; Gunjakar et al., 2011, 2013a, 2013b; Li et al., 2013). In addition to a large number of functional guest anions, the host LDH lattice could be modified with various

divalent and trivalent transition metal cations to induce new nanohybrids with unusual physicochemical properties and desired functions (Evans et al., 1996; Barriga et al., 1998; Leroux et al., 2001; Gago et al., 2005). In the case of LDHs and their nanohybrids, XAS has been used to study not only the local order and oxidation state within metal hydroxide layers but also the coordination environment around the metal atom in molecular cluster anions intercalated within LDHs (Moggridge et al., 1994; Defontaine et al., 2004; Arias et al., 2013; Okada et al., 1997; Huang et al., 2012; Vaysse et al., 2002; Sousa et al., 2006; Monteiro et al., 2008).

For example, the distribution and the upper limit of atomic fraction of Ni^{2+} and Al^{3+} cations in $Ni_{(1-x)}Al_x(OH)_2$ (terephthalate)$_{x/2}$, were evaluated, depending on x ranges of 0.3–0.8 at
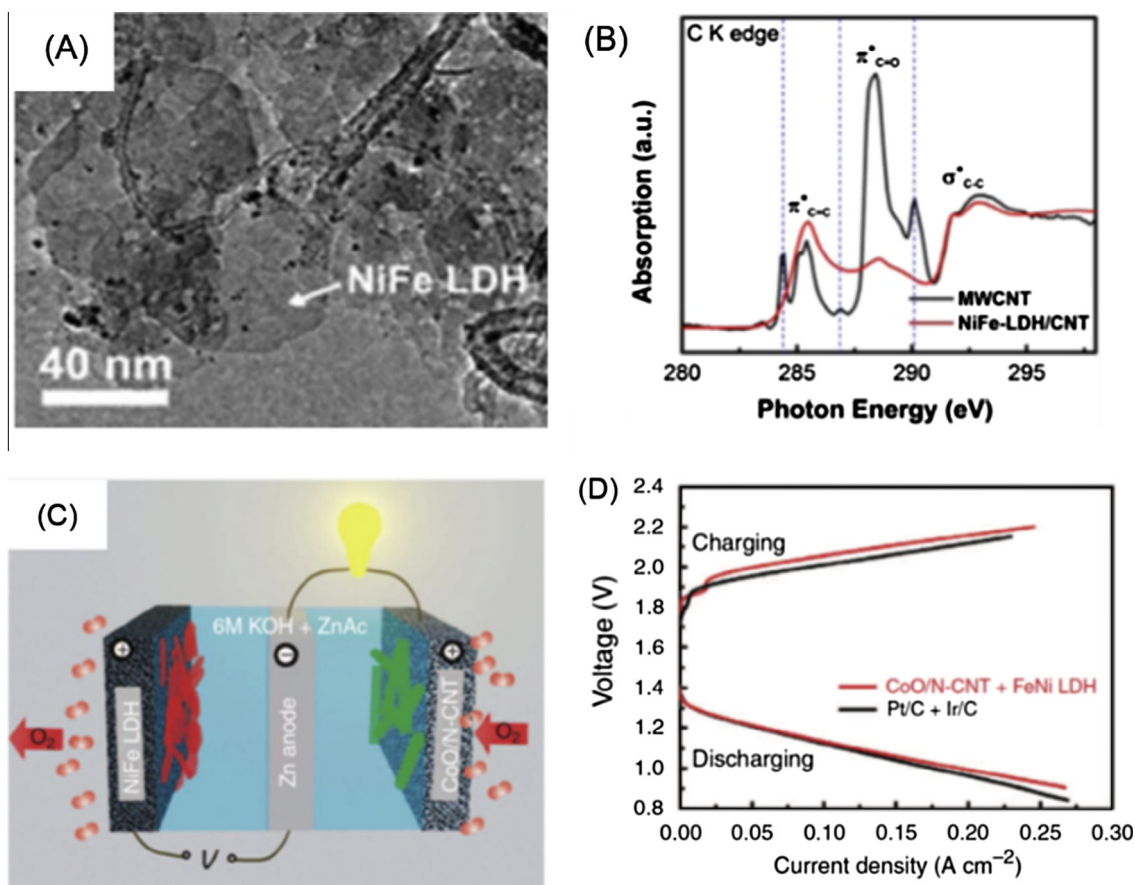
Figure 11 (A) TEM image and (B) C K-edge XANES spectra of Ni–Fe LDH/CNT. Reprinted from reference Gong et al. (2013)). Copyright 2013 American Chemical Society. (C) A schematic of the rechargeable Zn–air battery in a tri-electrode configuration and (D) charge and discharge polarization curves of the tri-electrode Zn–air battery. Reprinted from reference Li et al. (2013). Copyright 2013 Nature Publishing Group.

the Ni K-edge along with the simulated spectra (Kim et al., 2012). A decrease in peak intensity for the second nickel coordination shell was observed with the increase of Al^{3+} contents due to the replacement of Ni^{2+} ions in the hydroxide lattice by Al^{3+} ones, indicating an upper limit of ∼0.6 for the atomic fraction of Al^{3+} at the second nickel coordination sphere.

Woo et al. (2011b) prepared a series of mixed valent Zn^{2+}–Co^{2+}/Co^{3+} LDHs and their exfoliated nanosheets for electrode application, and confirmed the chemical bonding nature around cobalt ions and the oxidation state of Co^{2+}/Co^{3+} in the pristine Zn–Co LDHs and the post-calcined samples at the Co K-edge XANES. It was also found that the edge-position of as-prepared Zn–Co LDHs was higher than that of CoO but lower than that of $LiCoO_2$, indicating the mixed oxidation states of Co^{2+}/Co^{3+} (Fig. 9(A)). Furthermore, Zn–Co LDHs showed a weak peak (P) in the pre-edge region and the others (A and B) in the main-edge one, indicating that the octahedral symmetry of the cobalt ions was remained unchanged in the LDH lattice. The weak peak P is commonly proportional to the degree of distortion from regular octahedral symmetry, which corresponds to the dipole-forbidden $1s \rightarrow 3d$ transition. The features, A and B of the Zn–Co LDHs, were normally originated from the dipole-allowed $1s \rightarrow 4p$ transitions in the main-edge region.

As shown in Fig. 9(B), a stable colloidal suspensions of Zn–Co LDH could also be realized thanks to the exfoliation of lamellar material into individual nanosheets. According to the galvanostatic charge–discharge cycling, the Zn–Co LDH film exhibited a large discharge capacity of ∼170 F g^{-1}, with good capacitance retention. From the pseudo-capacitance behavior, one can expect that those mixed valent Zn–Co LDHs with porous structure would be applicable as the secondary building blocks to improve the electrode performance.

A similar study was also made to explore the oxidation state and the local symmetry of transition metal in LDHs and to rationalize an enhanced photocatalytic activity of ZnCr LDH systems (Gunjakar et al., 2011, 2013a, 2013b). In case of the self-assembly of positively-charged ZnCr 2D nanosheets and negatively-charged titanate 2D nanosheets, highly mesoporous nanohybrids (ZCT) with layer-by-layer ordered structure was realized with an improved chemical stability (Gunjakar et al., 2011). According to the ratios of layered titanate/layered ZnCr LDH with 0.91, 1.16 and 1.46 denoted as ZCT-1, ZCT-2, and ZCT-3, each specific surface area was determined as 67, 86, and 104 m^2 g^{-1}, respectively. From the spectral feature and the edge position at the Zn K-edge and the Cr K-edge XANES for the ZCT nanohybrids (Fig. 10(A)), a negligible change was observed in terms of the

crystal structure and the symmetry of Cr^{3+} ions in octahedral symmetry of LDHs even after hybridization. They observed that all of the ZCT nanohybrids maintained weak intensity of pre-edge peak (*P*) in accordance with the typical dipole-forbidden $1s \rightarrow 3d$ transition. Moreover, three features (A, B, and C) were commonly observed in the main-edge region through dipole-allowed $1s \rightarrow 4p$ transitions. As shown in Fig. 10(B), the ZCT nanohybrid showed very high photocatalytic activity for the visible light-induced O_2 generation with a rate of 1.18 mmol $h^{-1} g^{-1}$.

More recently, Gong et al. (2013) reported a NiFe LDH–CNT nanohybrid for electrocatalytic water oxidation and advanced metal–air battery system. The solvothermal synthesis of ultrathin NiFe LDH on multi-walled CNT resulted in the formation of highly active, durable, and cost-effective electrocatalysts for an oxygen evolution reaction (OER) in alkaline medium. Interaction between NiFe LDH and CNTs, afforded by direct nucleation and crystal growth of LDH on the functional groups on CNTs, contributed to the optimal OER activity of the NiFe LDH–CNT nanohybrid (Fig. 11(A)). The XANES spectra at the carbon K-edge showed a remarkable change in carbonyl π^* peak intensity after hybridization (Fig. 11(B)). This is surely due to the formation of covalent M–O–C (M = Ni or Fe) bonding by direct nucleation and crystal growth of LDH on the surface of functionalized CNT, and therefore, such a covalently bound nanohybrid could facilitate the charge transport resulting in high OER activity and stability.

In the meantime, Li et al. (2013) developed an advanced zinc–air battery consisted of the NiFe LDH–CNT nanohybrid electrode, which showed higher catalytic activity and durability than precious metal Pt/C and Ir/C composite catalysts. The rechargeable Zn–air batteries with a tri-electrode configuration with OER catalyst, NiFe LDH–CNT, and ORR catalyst, CoO/N–CNT, for cathode material showed a very small charge–discharge voltage polarization of $\sim$0.70 V at 20 mA cm^{-2}, high reversibility and stability over long term charge and discharge cycles (Fig. 11(C) and (D)).

5. Summary

A large variety of molecules with cationic or anionic charge, metal ions, metal oxide clusters, polymer, and even 2D oxide nanosheets have been incorporated within the interlayer space of layered silicates (clays) or LDHs to form layered or porous nanohybrids. In order to trace the intercalation processes and subsequent pillaring reaction upon post-calcination, and/or exfoliation–reassembling ones, it is necessary to investigate the correlation between chemical bonding nature and electronic structure of constituting elements, i.e. changes in local symmetry, chemical, and electronic environments of both guest species and host lattices, which are in turn closely related to their physicochemical functions. In this regard, X-ray diffraction (XRD) and X-ray spectroscopic (XANES and EXAFS) analyses could be considered as very powerful tools not only to quantitatively probe structural and electronic evolutions for specific elements even in X-ray amorphous solids but also to propose structural models for poorly crystalline samples such as intercalative nanohybrids. We hope that highlighted examples in this review would be very introductive for the readers who are currently working on low dimensional and/or poorly crystalline solids such as intercalation compounds and molecular composites.

References

Adams, J.M., Thomas, J.M., Walters, M.J., 1976. J. Chem. Soc. Dalton, 112.

Adams, J.M., 1974. J. Chem. Soc. Dalton, 2286.

Alvim, R.S., Miranda, C.R., 2015. Phys. Chem. Chem. Phys. 17, 4952.

Ankudinov, A.L., Ravel, B., Rehr, J.J., Conradson, S.D., 1998. Phys. Rev. B 58, 7565.

Argüelles, A., Leoni, M., Blanco, J.A., Marcos, C., 2010. Am. Mineral. 95, 126.

Arias, S., Eon, J.G., San Gil, R.A.S., Licea, Y.E., Palacio, L.A., Faro Jr., A.C., 2013. Dalton Trans. 42, 2084.

Auerbach, S.M., Carrado, K.A., Dutta, P.K. (Eds.), 2004. Handbook of Layered Materials. CRC Press. Marcel Dekker Inc.

Barriga, C., Jones, W., Malet, P., Rives, V., Ulibarri, M.A., 1998. Inorg. Chem. 37, 1812.

Bergaya, F., Lagaly, G. (Eds.), 2013. Handbook of Clay Science, 2nd ed. Elsevier, Amsterdam.

Besserguenev, A.V., Fogg, A.M., Francis, R.J., Price, S.J., O'Hare, D., 1997. Chem. Mater. 9, 241.

Bornholdt, K., Corker, J.M., Evans, J., Rummey, J.M., 1991. Inorg. Chem. 30, 1.

Brendlé, J.M., Khouchaf, L., Baron, J., Le Dred, R., Tuilier, M.H., 1997. Microporous Mater. 11, 171.

Bruce, D.W., O'Hare, D. (Eds.), 1997. Inorganic Materials. John Wiley & Sons Ltd. West Sussex, England.

Carvalho, H.W.P., Santilli, C.V., Briois, V., Pulcinelli, S.H., 2013. RSC Adv. 3, 22830.

Choy, J.H., Kim, D.K., Hwang, S.H., Demazeau, G., Jung, D.Y., 1995. J. Am. Chem. Soc. 117, 8557.

Choy, J.H., Hong, S.T., Choi, K.S., 1996. J. Chem. Soc., Faraday Trans. 92, 1051.

Choy, J.H., Kwak, S.Y., Han, Y.S., Kim, B.W., 1997a. Mater. Lett. 33, 143.

Choy, J.H., Hwang, S.J., Park, N.G., 1997b. J. Am. Chem. Soc. 119, 1624.

Choy, J.H., Kim, D.K., Park, J.C., Choi, S.N., Kim, Y.J., 1997c. Inorg. Chem. 36, 189.

Choy, J.H., Kim, B.W., Yoon, J.B., Park, J.C., 1998a. Mol. Cryst. Liq. Cryst. 311, 303.

Choy, J.H., Kim, J.T., Yoon, J.B., Kim, D.K., 1998b. Mol. Cryst. Liq. Cryst. 311, 315.

Choy, J.H., Park, J.H., Yoon, J.B., 1998c. J. Phys. Chem. B 31, 5991.

Choy, J.H., Kim, J.Y., Kim, S.J., Sohn, J.S., Han, O.H., 2001a. Chem. Mater. 13, 906.

Choy, J.H., Jung, H., Yoon, J.B., 2001b. J. Synchrotron. Radiat. 8, 599.

Choy, J.H., Yoon, J.B., Park, J.H., 2001c. J. Synchrotron. Radiat. 8, 782.

Choy, J.H., Jung, H., Han, Y.S., Yoon, J.B., Shul, Y.G., Kim, H.J., 2002. Chem. Mater. 14, 3823.

Choy, J.H., Yoon, J.B., Jung, H., Park, J.H., 2003. J. Mater. Chem. 13, 557.

Choy, J.H., 2004. J. Phys. Chem. Solids 65, 373.

Choy, J.H., Choi, S.J., Oh, J.M., Park, T., 2007. Appl. Clay Sci. 36, 122.

Claret, F., Sakharov, B.A., Drits, V.A., Velde, B., Meunier, A., Griffault, L., Lanson, B., 2004. Clays Clay Miner. 52, 515.

Costantino, U., Marmottini, F., Nocchetti, M., Vivani, R., 1998. Eur. J. Inorg. Chem., 1439.

Cunha, V.R.R., Petersen, P.A.D., Gonçalves, M.V., Petrilli, H.M., Taviot-Guého, C., Leroux, F., Temperini, M.L.A., Constantino, V.R.L., 2012. Chem. Mater. 24, 1415.

Defontaine, G., Michot, L.J., Bihannic, I., Ghanbaja, J., Briois, V., 2004. Langmuir 20, 11213.

Delatorre, P., de Azevedo Jr., W.F., 2001. J. Appl. Cryst. 34, 658.

Ennadi, A., Legrouri, A., Roy, A.D., Besse, J.P., 2000. J. Solid State Chem. 152, 568.

Evans, J., Pillinger, M., Zhang, J., 1996. J. Chem. Soc., Dalton Trans., 2963

Fogg, A.M., Dunn, J.S., O'Hare, D., 1998. Chem. Mater. 10, 356.

Fujita, T., Iyi, N., Kosugi, T., Ando, A., Deguchi, T., Sota, T., 1997. Clays Clay Miner. 45, 77.

Gago, S., Pillinger, M., Ferreira, R.A.S., Carlos, L.D., Santos, T.M., Gonçalves, I.S., 2005. Chem. Mater. 17, 5803.

Gomes, A.C., Bruno, S.M., Gamelas, C.A., Valente, A.A., Abrantes, M., Gonçalves, I.S., Romão, C.C., Pillinger, M., 2013. Dalton Trans. 42, 8231.

Gong, M., Li, Y., Wang, H., Liang, Y., Wu, J.Z., Zhou, J., Wang, J., Regier, T., Wei, F., Dai, H., 2013. J. Am. Chem. Soc. 135, 8452.

Gunjakar, J.L., Kim, T.W., Kim, H.N., Kim, I.Y., Hwang, S.J., 2011. J. Am. Chem. Soc. 133, 14998.

Gunjakar, J.L., Kim, I.Y., Lee, J.M., Lee, N.S., Hwang, S.J., 2013a. Energy Environ. Sci. 6, 1008.

Gunjakar, J.L., Kim, T.W., Kim, I.Y., Lee, J.M., Hwang, S.J., 2013b. Sci. Rep. 3, 2080.

Gunjakar, J.L., Kim, I.Y., Lee, J.M., Jo, Y.K., Hwang, S.J., 2014. J. Phys. Chem. C 118, 3847.

Han, Y.S., Matsumoto, H., Yamanaka, S., 1997. Chem. Mater. 9, 2013.

Han, Y.S., Choy, J.H., 1998. J. Mater. Chem. 8, 1459.

Han, Y.S., Yamanaka, S., Choy, J.H., 1999. J. Solid State Chem. 144, 45.

Hitzky, E.R., Aranda, P., Darder, M., Rytwo, G., 2010. J. Mater. Chem. 20, 9306.

Huang, Z., Wu, P., Zhang, X., Wang, X., Zhu, N., Wu, J., Li, P., 2012. Appl. Clay Sci. 65, 87.

Hur, S.G., Kim, T.W., Hwang, S.J., Hwang, S.H., Yang, J.H., Choy, J.H., 2006. J. Phys. Chem. B 110, 1599.

Ibers, J.A., Hamilton, W.C. (Eds.), 1989. International Tables for X-ray Crystallography, vol. 4. International Union of Crystallography by Kluwer Academic Publishers, Boston.

Illaik, A., Taviot-Guého, C., Lavis, J., Commerecuc, S., Verney, V., Leroux, F., 2008. Chem. Mater. 20, 4854.

Intissar, M., Jumas, J.C., Besse, J.P., Leroux, F., 2003. Chem. Mater. 15, 4625.

Itoh, T., Shichi, T., Takahashi, H., Inui, Y., Takagi, K., 2005. J. Phys. Chem. B 109, 3199.

Jung, H., Paek, S.M., Yoon, J.B., Choy, J.H., 2007. J. Porous Mater. 14, 369.

Káfuňková, E., Taviot-Guého, C., Bezdička, P., Klementová, M., Kovář, P., Kubát, P., Mosinger, J., Pospíšil, M., Lang, K., 2010. Chem. Mater. 22, 2481.

Kakinoki, T., Komura, Y., 1965. Acta Crystallogr. 17, 579.

Kamada, K., Kang, J.H., Paek, S.M., Choy, J.H., 2012. J. Phys. Chem. Solids 73, 1478.

Kanamaru, F., Vand, V., 1970. Am. Mineral. 55, 1550.

Kawabata, T., Kato, M., Mizugaki, T., Ebitani, K., Kaneda, K., 2005. Chem. Eur. J. 11, 288.

Kennard, C.H.L., 1972. J. Appl. Cryst. 5, 382.

Kim, S.J., Lemaux, S., Demazeau, G., Kim, J.Y., Choy, J.H., 2001. J. Am. Chem. Soc. 123, 10413.

Kim, T.W., Ha, H.W., Paek, M.R., Hyun, S.H., Paek, I.H., Choy, J.H., Hwang, S.J., 2008. J. Phys. Chem. C 112, 14853.

Kim, T.H., Heo, I., Paek, S.M., Park, C.B., Choi, A.J., Lee, S.H., Choy, J.H., Oh, J.M., 2012. Bull. Korean Chem. Soc. 33, 1845.

Kim, M.H., Park, D.H., Yang, J.H., Choy, Y.B., Choy, J.H., 2013. Int. J. Pharm. 444, 120.

Kuks, W.K., Huh, Y.D., 1997. J. Mater. Chem. 7, 1933.

Ladd, M.F.C., Palmer, R.A. (Eds.), 1994. Structure Determination by X-ray Crystallography. Plenum Press, New York.

Lavela, P., Morales, J., Tirado, J.L., 1996. J. Solid State Chem. 124, 238.

Lee, S.R., Park, M., Han, Y.S., Hwang, S.H., Choy, J.H., 2005. J. Phys. Chem. B 109, 9432.

Lee, B.I., Lee, K.S., Lee, J.H., Lee, I.S., Byeon, S.H., 2009. Dalton Trans., 2490

Leroux, F., Pagano, M.A., Intissar, M., Chauviére, S., Forano, C., Besse, J.P., 2001. J. Mater. Chem. 11, 105.

Leroux, F., Taviot-Guého, C., 2005. J. Mater. Chem. 15, 3628.

Li, Y., Gong, M., Liang, Y., Feng, J., Kim, J.E., Wang, H., Hong, G., Zhang, B., Dai, H., 2013. Nat. Commun. 4, 1805.

Lim, H., Yoon, S.I., Kim, G., Jang, A.R., Shin, H.S., 2014. Chem. Mater. 26, 4891.

Lytle, F.W., 1999. J. Synchrotron. Radiat. 6, 123.

Malferrari, D., Brigatti, M.F., Marcelli, A., Chu, W., Wu, Z., 2008. Micropor. Mesopor. Mater. 107, 128.

Marangoni, R., Taviot-Guého, C., Illaik, A., Wypych, F., Leroux, F., 2008. J. Colloid Interf. Sci. 326, 366.

McCarty, V.A., Sakharov, D.K., Drits, V.A., 2008. Clays Clay Miner. 56, 359.

Moggridge, G.D., Parent, P., Tourillon, G., 1994. Clays Clay Miner. 42, 462.

Monteiro, B., Gago, S., Paz, F.A.A., Bilsborrow, R., Gonçalves, I.S., Pillinger, M., 2008. Inorg. Chem. 47, 8674.

Mudhivarthi, V.K., Bhambhani, A., Kumar, C.V., 2007. Dalton Trans., 5483

Mustre de Leon, J., Rehr, J.J., Zabinsky, S.I., 1991. Phys. Rev. B 44, 4146.

Newville, M., Livins, P., Yacoby, Y., Rehr, J.J., Stern, E.A., 1993. Phys. Rev. B 47, 14126.

O'Day, P.A., Rehr, J.J., Zabinsky, S.I., Brown Jr., G.E., 1994. J. Am. Chem. Soc. 116, 2938.

Ogawa, M., Kuroda, K., 1995. Chem. Rev. 95, 399.

Oh, J.M., Biswick, T.T., Choy, J.H., 2009. J. Mater. Chem. 19, 2553.

Oh, J.M., Park, D.H., Choy, J.H., 2011. Chem. Soc. Rev. 40, 583.

Okada, K., Matsushita, F., Hayashi, S., 1997. Clay Miner. 32, 299.

Park, H.M., Kim, T.W., Hwang, S.J., Choy, J.H., 2006. Bull. Korean Chem. Soc. 27, 1323.

Park, D.H., Hwang, S.J., Oh, J.M., Yang, J.H., Choy, J.H., 2013. Prog. Polym. Sci. 38, 1442.

Paek, S.M., Jung, H., Lee, Y.J., Park, M., Hwang, S.J., Choy, J.H., 2006a. Chem. Mater. 18, 1134.

Paek, S.M., Jang, J.U., Hwang, S.J., Choy, J.H., 2006b. J. Phys. Chem. Solids 67, 1020.

Paek, S.M., Oh, J.M., Choy, J.H., 2011. Chem. Asian J. 6, 324.

Pecharsky, V.K., Zavalij, P.Y. (Eds.), 2005. Fundamentals of Powder Diffraction and Structural Characterization of Materials. Springer, New York.

Plançon, A., Drits, V.A., 1999. Clays Clay Miner. 48, 57.

Rehr, J.J., Mustre de Leon, J., Zabinsky, S.I., Albers, R.C., 1991. J. Am. Chem. Soc. 113, 5135.

Rehr, J.J., Albers, R.C., 2000. Rev. Mod. Phys. 72, 621.

Rehr, J.J., Kas, J.J., Vila, F.D., Prange, M.P., Jorissen, K., 2010. Phys. Chem. Chem. Phys. 12, 5503.

Rives, V. (Ed.), 2001. Layered Double Hydroxides: Present and Future. Nova Science Publishers Inc, New York.

Sato, M., 1987. Clay Sci. 7, 41.

Sham, T.K., 1986. Acc. Chem. Res. 19, 99.

Sousa, F.L., Pillinger, M., Ferreira, R.A.S., Granadeiro, C.M., Cavaleiro, A.M.V., Rocha, J., Carlos, L.D., Trindade, T., Nogueira, H.I.S., 2006. Eur. J. Inorg. Chem., 726

Su, Z.W., Coppens, P., 1997. Acta. Cryst. A53, 749.

Takahama, K., Yokoyama, M., Hirao, S., Yamanaka, S., Hattori, M., 1992. J. Mater. Sci. 27, 1297.

Tateyama, H., Noma, H., Nishimura, S., Adachi, Y., Ooi, M., Urabe, K., 1998. Clays Clay Miner. 46, 245.

Taviot-Guého, C., Feng, Y., Faour, A., Leroux, F., 2010. Dalton Trans. 39, 5994.

Thevenot, F., Szymanski, R., Chaumette, P., 1989. Clays Clay Miner. 37, 396.

Thompson, J.G., Cuff, C., 1985. Clays Clay Miner. 33, 490.

Uehara, M., Yamazaki, A., Umezawa, T., Takahashi, K., Tsutsumi, S., 1999. Clays Clay Miner. 47, 726.

Vaysse, C., Demourgues, L.G., Demourgues, A., Delmas, C., 2002. J. Solid State Chem. 167, 59.

Vicente, C.P., Tirado, J.L., Adouby, K., Jumas, J.C., Touré, A.A., Kra, G., 1999. Inorg. Chem. 38, 2131.

Wang, Q., Hanson, J.C., Frenkel, A.I., 2008. J. Chem. Phys. 129, 234502.

Wang, Q., O'Hare, D., 2012. Chem. Rev. 112, 4124.

Whittingham, M.S., Jacobson, A.J. (Eds.), 1982. Intercalation Chemistry. Academic Press, New York.

Williams, G.R., Norquist, A.J., O'Hare, D., 2004. Chem. Mater. 16, 975.

Williams, G.R., O'Hare, D., 2006. J. Mater. Chem. 16, 3065.

Williams, G.R., Fogg, A.M., Sloan, J., Tavio-Guého, C., O'Hare, D., 2007. Dalton Trans., 3499

Woo, M.A., Kim, T.W., Paek, M.J., Ha, H.W., Choy, J.H., Hwang, S.J., 2011a. J. Solid State Chem. 184, 171.

Woo, M.A., Song, M.S., Kim, T.W., Kim, I.Y., Ju, J.Y., Lee, Y.S., Kim, S.J., Choy, J.H., Hwang, S.J., 2011b. J. Mater. Chem. 21, 4286.

Yamanaka, S., Inoue, Y., Hattori, M., Okumura, F., Yoshiikawa, M., 1992. Bull. Chem. Soc. Jpn. 65, 2494.

Yang, J.H., Han, Y.S., Choy, J.H., Tateyama, H., 2001. J. Mater. Chem. 11, 1305.

Yang, J.H., Han, Y.S., Park, M., Park, T., Hwang, S.J., Choy, J.H., 2007. Chem. Mater. 19, 2679.

Yang, J.H., Lee, H.S., Paek, S.M., Han, Y.S., 2011. Chem. Lett. 40, 1242.

Yang, J.H., Jung, H., Kim, S.Y., Choy, J.H., 2013. J. Nanosci. Nanotechnol. 13, 7331.

Yang, J.H., Piao, H., Vinu, A., Elzatahry, A.A., Paek, S.M., Choy, J.H., 2015. RSC Adv. 5, 8210.

Young, R.A. (Ed.), 1993. The Rietveld Method. Oxford University Press, Oxford.

Yu, J., Martin, B.R., Clearfield, A., Luod, Z., Sun, L., 2015. Nanoscale 7, 9448.

Zeng, Z., Matuschek, D., Studer, A., Schwickert, C., Pöttgen, R., Eckert, H., 2013. Dalton Trans. 42, 8585.